

# Effect of Al Content on Abnormal Grain Growth and Superelasticity in Fe–Mn–Al–Cr–Ni Shape Memory Alloys with Near-Zero Temperature-Dependence of Transformation Stress

Ji Xia<sup>1</sup> · Toru Hoshi<sup>1</sup> · Xiao Xu<sup>1</sup> · Toshihiro Omori<sup>1</sup>  · Ryosuke Kainuma<sup>1</sup>

Received: 29 June 2021 / Revised: 20 August 2021 / Accepted: 20 August 2021 / Published online: 8 September 2021  
© ASM International 2021

**Abstract** The solvus temperature of face-centered cubic (FCC) phase in Fe–34Mn– $x$ Al–4Cr–7.5Ni ( $x = 13, 14,$  and  $15$ ) shape memory alloys with different Al contents, and their abnormal grain growth and superelasticity at various temperatures were evaluated. With increasing Al content, the solvus temperature of the FCC phase decreased and the FCC precipitates became finer. Whereas cyclic heat treatment induced abnormal grain growth (AGG) in all samples, large grains were obtained more easily in the alloys with higher Al content. The critical stress for martensitic transformation increased with increasing Al content. The  $x = 14$  alloy is the optimal composition considering grain growth and superelasticity. The newly developed Fe–34Mn–14Al–4Cr–7.5Ni alloy, in which single-crystal can easily be fabricated by AGG, exhibited superelasticity at temperatures ranging from  $-263$  °C (10 K) to  $27$  °C (300 K), with a very small temperature-dependence of the critical stress, comparable to that of conventional Fe–34Mn–13.5Al–3Cr–7.5Ni alloy.

**Keywords** Ferrous shape memory alloy · Microstructure control · Abnormal grain growth · Superelasticity

## Introduction

Iron-based shape memory alloys have attracted the attention of researchers owing to their lower cost and better workability compared to conventional Ni–Ti-based alloys. Fe-based shape memory alloys that exhibit reversible martensitic transformation can be roughly classified into four groups: (i) Fe-noble metal-based alloys, such as Fe–Pt [1] and Fe–Pd [2], (ii) Fe–Ni–Co-based alloys, such as Fe–Ni–Co–Ti [3], Fe–Ni–Co–Al–Ta–B [4], Fe–Ni–Co–Al–Nb–B [5], and Fe–Ni–Co–Al–Ti–B [6], (iii) face-centered cubic (FCC) Fe–Mn-based alloys, such as Fe–Mn–Si [7–9], and (iv) body-centered cubic (BCC) Fe–Mn-based alloys, such as Fe–Mn–Ga [10, 11] and Fe–Mn–Al–Ni [12]. Among them, the Fe–Ni–Co-based and BCC Fe–Mn-based alloys can exhibit remarkable superelasticity. In the case of Fe–Ni–Co–Al-based polycrystalline alloys [4–6], low-energy grain boundaries, obtained by heavy cold-rolling and subsequent heat treatment, are necessary to suppress grain boundary precipitation to achieve good ductility and superelasticity. Thus, the applications of these alloys are restricted to thin sheet samples [13–16]. Although the single crystals of these alloys show superior superelasticity [17–19], the fabrication cost through traditional method is expensive.

The Fe–Mn–Al–Ni shape memory alloy was developed from a non-thermoelastic Fe–Mn–Al ternary alloy [20]. The addition of Ni introduced ordered coherent B2 precipitates into the disordered BCC (A2) matrix and ensured thermoelastic martensitic transformation [21]. This strategy is similar to the development of Fe–Ni–Co–Ti [3] and Fe–Ni–Co–Al [4], where the coherent L1<sub>2</sub> phase precipitates into the FCC matrix. The Fe–Mn–Al–Ni shape memory alloy exhibits superelasticity over a wide temperature range owing to the small entropy change during martensitic

---

This article is part of a special topical focus in Shape Memory and Superelasticity on Fe-Based Shape Memory Alloys. This issue was organized by Dr. Toshihiro Omori and Dr. Ryosuke Kainuma, Tohoku University.

---

✉ Toshihiro Omori  
omori@material.tohoku.ac.jp

<sup>1</sup> Department of Materials Science, Graduate School of Engineering, Tohoku University, Aoba-yama 6-6-02, Sendai 980-8579, Japan

transformation [12, 22, 23]. The superelastic performance is affected by the grain size relative to the cross-sectional area of the sample [12, 24, 25], as well as the size and volume fraction of the precipitate [26–28] and crystallographic orientation [29–31]. Abnormal grain growth (AGG) induced by cyclic heat treatment [32, 33] in this alloy system [34] also promotes practical application of the alloy. It has been reported that cyclic heat treatment between the BCC single-phase and BCC + FCC two-phase regions results in a subgrain structure in the BCC phase and that an AGG occurs driven by the sub-boundary energy. A large single crystal can be obtained by cyclic heat treatment [35], which means that the Fe–Mn–Al–Ni alloy is currently a promising choice for large component applications, including use in civil engineering [36].

The composition of the originally reported Fe–34Mn–15Al–7.5Ni (at%) alloy [12] has been tuned to address several practical problems, such as the formation of cracks during final quenching, the difficulty in fabricating much larger single-crystal samples by AGG, and insufficient superelasticity. To solve the problem of crack formation upon water quenching, Vollmer et al. added Ti to the Fe–Mn–Al–Ni alloy to reduce its quenching sensitivity [37]. Because Ti is a BCC stabilizer in this alloy, the formation of the FCC phase was greatly suppressed, and an almost single BCC phase with thin FCC phase layers at the grain boundaries could be obtained after air cooling. Further investigations revealed that the driving force for AGG can be enhanced by Ti addition, and large single crystals could be easily obtained [35]. Another report showed that Al addition has the same effect on promoting AGG by reducing the solvus temperature of the FCC phase [38]. To optimize the superelasticity, Vallejos et al. adjusted the Al and Ni content of the alloy by considering the miscibility gap, where the as-quenched samples exhibited excellent superelasticity [39]. Recently, Walnsch et al. conducted thermodynamic calculations for the Fe–Mn–Al–Ni alloy system [40] and proposed that the  $D0_3$  ordered parent phase may transform into the  $D0_{22}$  martensite phase in the Mn-rich Fe–Mn–Al–Ni alloy [41]. These studies have contributed to more comprehensive understanding of this alloy system.

Cr is well-known as an element that improves the oxidation and corrosion resistance of alloys. Both Al and Cr are BCC stabilizers at 1200 °C, as indicated in the Fe–Mn–Al [42] and Fe–Mn–Cr [43] ternary phase diagrams. Based on this information and the compositions of the quaternary alloys, we fabricated Fe–34Mn–(15– $x$ /2)Al– $x$ Cr–7.5Ni single crystals and examined their mechanical properties over a wide temperature range from 10 to 300 K [44, 45]. Cr addition can change the temperature-dependence of the critical stress from positive to negative in stress-induced martensitic (SIM) transformation [45]. AGG and

superelasticity were confirmed for Fe–Mn–Al–Cr–Ni alloys, but the effects of each alloying element, except for Cr, on the properties of the quaternary system are still unknown.

In this study, the effects of the Al content on the AGG and the superelastic properties of the Fe–Mn–Al–Cr–Ni alloy are investigated to achieve higher efficiency for single-crystal fabrication and good superelastic performance, including near-constant critical stress over a wide temperature range. Because near-constant critical stress temperature dependence is expected to be obtained with 3 to 4 at.% Cr [45], Fe–34Mn– $x$ Al–4Cr–7.5Ni ( $x = 13, 14, \text{ and } 15$ ) alloys were selected based on the Fe–34Mn–15Al–7.5Ni alloy.

## Materials and Methods

### Sample Preparation

Fe–34Mn–(13, 14, and 15)Al–4Cr–7.5Ni (at.%) alloys were fabricated from high-purity metals by high-frequency induction melting under argon atmosphere. For simplicity, these samples are referred to as 13Al, 14Al, and 15Al in the following text. 13Al is the composition in line with the previous alloy design, Fe–34Mn–(15– $x$ /2)Al– $x$ Cr–7.5Ni [44, 45]. The samples were hot-rolled to approximately 2 mm (90% thickness reduction) and 4 mm (80% thickness reduction) in thickness at 1200 °C. The thick strips were used for single-crystal fabrication for the compression tests, while the thin strips were used for the other measurements. Solution heat treatment (SHT) was conducted at 1200 °C for 30 min in the BCC single-phase region, followed by water quenching.

### Measurement of Solvus Temperature

The FCC solvus temperature of each alloy was determined by differential scanning calorimetry (DSC, Netzsch, DSC404C), where the mass of the samples was approximately 120–180 mg. The SHT samples were heated from 20 °C to 1300 °C, held for 1 min, and then cooled to 20 °C at a rate of 10 °C/min. To eliminate reactions from metastable phases, two runs were conducted on the same sample, and the second heating segment was used to determine the solvus temperature.

### X-ray Diffraction Measurements

X-ray diffraction measurements were carried out to identify the crystal structures of the phases that appeared during the heating process. The as-rolled 13Al alloy was heated from room temperature to 1000 °C, 1100 °C, and 1200 °C

at a rate of 10 °C/min, followed by water quenching. These samples were then polished with up to 600 grit SiC paper, followed by ultrasonic cleaning in ethanol. X-ray diffraction patterns of the samples were obtained using an X-ray diffractometer (D8 advance, Bruker) with a Cu-K $\alpha$  radiation source, where the rotation speed was 15 rpm and the 2 $\theta$  angle was scanned from 20° to 120° with a step size of 0.02°.

### Microstructural Observation

The microstructure was observed using optical microscope (Axioplan2, Zeiss). To prevent the crack formation during final quenching, the samples to be quenched from the BCC single-phase region were wrapped in oxidized molybdenum foil (thickness: 0.05 mm) and then sealed in a quartz tube [46]. After heat treatment, the samples were polished by diamond powders up to 0.25  $\mu\text{m}$  and etched using the 10% Nital solution (10% nitric acid and 90% ethanol in volume fraction).

To observe the morphology and size of the FCC phase and the subgrain structure in the BCC phase, the microstructures of the samples subjected to cyclic heat treatment were analyzed by electron backscattered diffraction (EBSD), operated at 25 kV with a probe current of 16  $\mu\text{A}$ . The details of the heat treatments are shown in the relevant figures. The inverse pole figure (IPF) and grain reference orientation deviation (GROD) maps were obtained using EBSD.

The microstructure of the B2 precipitate was characterized by conventional transmission electron microscopy (TEM) (JEM-2100, JEOL) using the SHT sample of these alloys. The sample was first parallel ground to a thickness of approximately 80  $\mu\text{m}$ , and punched to obtain small disks, followed by twin-jet electropolishing using an electrolyte consisting of 6% perchloric acid, 12% acetic acid, 12% ethylene glycol, and 70% ethanol.

### Compression Test

To evaluate the superelastic performance of the studied alloys, the incremental compression strain tests were conducted at room temperature using single-crystal samples. For fabrication of the single crystal, samples with a size of 4 mm  $\times$  4 mm  $\times$  50 mm were cut from the as-rolled strips, wrapped in oxidized Mo foil, and sealed in a quartz tube for cyclic heat treatment. The details of the cyclic heat treatment are presented in Fig. 1. Compared with the cyclic heat treatment in a previous report [34], a slow heating process starting at  $T_1$ , which is 10 °C lower than the FCC solvus temperature, was added to promote selective grain growth.

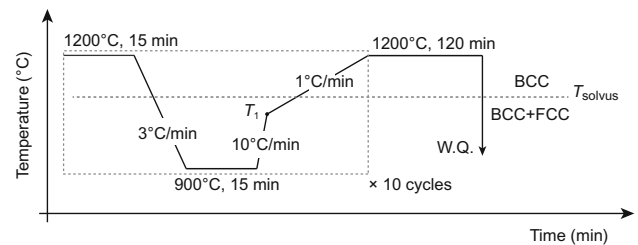


**Fig. 1** Cyclic heat treatment process used for single-crystal fabrication in this study, where  $T_1$  is a temperature 10 °C lower than the FCC solvus temperature,  $T_{\text{solvus}}$

The compression samples (about 2.5 mm  $\times$  2.5 mm  $\times$  6.0 mm) were cut from these large single crystals and no further aging heat treatment was conducted before the mechanical tests. The crystal orientation of the samples was measured by EBSD. Up to 6% strain was applied, with an increment of 1% in each cycle, using a universal testing machine (Shimadzu). The strain rate in the compression tests was  $5 \times 10^{-4} \text{ s}^{-1}$ . To evaluate the temperature-dependence of the critical stress in the 14Al alloy, the critical stress in a single-crystal sample was evaluated in the range of  $-263 \text{ }^\circ\text{C}$  (10 K) to  $27 \text{ }^\circ\text{C}$  (300 K) using another universal testing machine (Instron). The sample was first compressed at room temperature to confirm superelasticity, then cooled to  $-263 \text{ }^\circ\text{C}$  (10 K) and compressed during the heating process. The tests were conducted only once at each temperature to avoid cycling effect. The target compressive strain was approximately 1.6% in all tests, and the critical stress was determined using the 0.1% strain offset method.

## Results and Discussion

### Solvus Temperature

Figure 2a shows the DSC heating curves of the 13Al, 14Al, and 15Al alloys, where the endothermic reactions are indicated by arrows. Based on the X-ray diffraction patterns of samples quenched from 1000 °C and 1100 °C, 13Al has a two-phase structure of FCC and BCC phases, consistent with the microstructures shown in Fig. 2c. At 1200 °C, 13Al exhibited a single-phase microstructure. Therefore, the endothermic reactions in Fig. 2a are due to the FCC + BCC  $\rightarrow$  BCC transformation; the FCC solvus temperatures are summarized in Table 1. The solvus temperature of the 13Al alloy is comparable to that of the Fe–34Mn–15Al–7.5Ni alloy (1156 °C, [38]), and decreased with the addition of Al. This result is reasonable because Al is a BCC stabilizing element [42], and this tendency is consistent with that reported in the Fe–Mn–Al–Ni quaternary alloy [38].

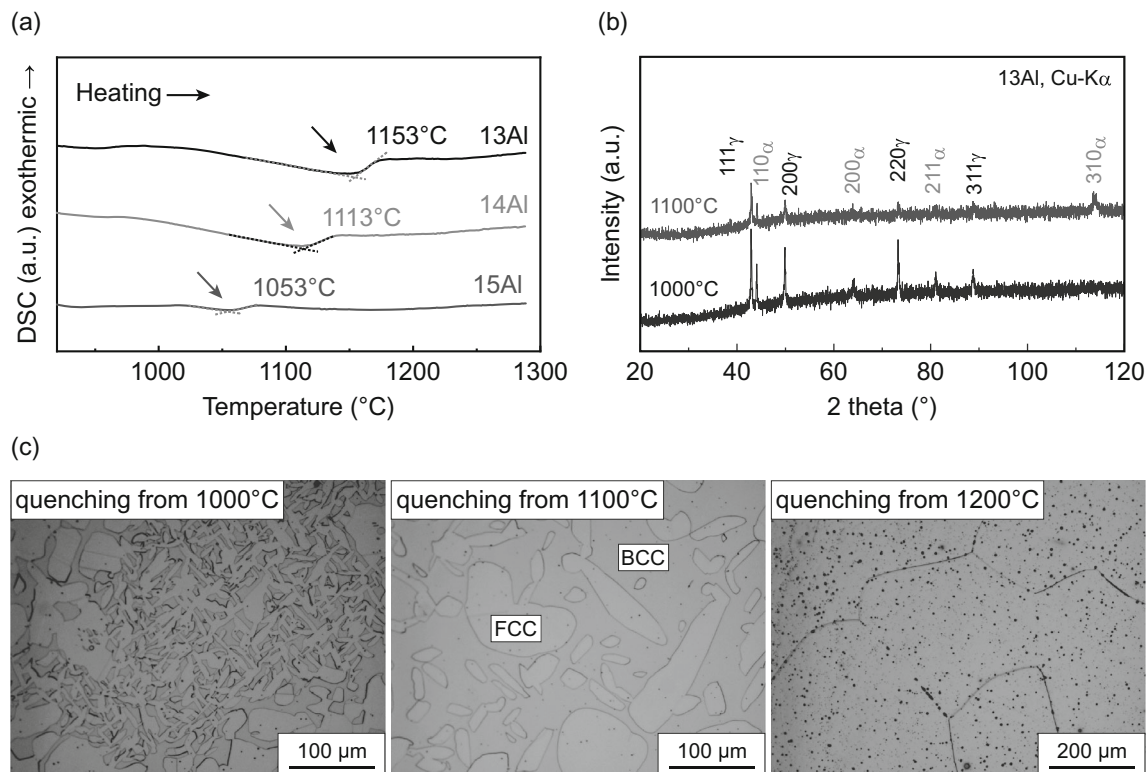


**Fig. 2** **a** Differential scanning calorimetry (DSC) heating curves for alloys studied in this work. Solvus temperatures of FCC phase are indicated by arrows. **b** X-ray diffraction patterns and **c** optical

microstructures of 13Al quenched from 1000 °C, 1100 °C, and 1200 °C during the heating process

**Table 1** Summary of FCC solvus temperature and FCC phase fraction at 900 °C for the alloys studied in this work. The volume fraction of the FCC phase was obtained from the phase map of EBSD measurements

Composition (at.%)	Solvus temperature (°C)	Volume fraction (%)
13Al	1153	76.8
14Al	1113	61.0
15Al	1053	43.5

### Abnormal Grain Growth

The IPF maps of the BCC and FCC two-phase microstructures obtained for the 13Al, 14Al, and 15Al samples cooled from 1200 °C, followed by annealing at 900 °C, are shown in Fig. 3. The alloys with a lower solvus temperature (i.e., a higher Al content) tended to have a finer FCC phase, where the 15Al alloy showed the finest FCC precipitates. According to the previous reports [33, 35, 38], smaller subgrain structures can be obtained with finer FCC precipitates, which results in a higher driving force for the AGG. In order to observe the microstructure before the migration of grain boundaries, the samples were quenched at  $T_2$ , which is 10 °C higher

than the FCC solvus temperature. Figure 4 shows the IPF and GROD maps of the alloys in the BCC phase quenched from  $T_2$  during the heating process from 900 °C. The subgrain microstructure can be clearly observed in the GROD maps. Although it is difficult to quantitatively determine the size of subgrains, at first glance, 15Al has the finest microstructure. This means that alloys with lower solvus temperature exhibit smaller subgrains.

The optical microstructures of the samples are shown in Fig. 5. At  $T_2$ , AGG was hardly observed, and the grain size distribution did not seem to be very different for the three alloys (Fig. 5b). Upon further heating to 1200 °C, some grains started to grow abnormally in the 14Al alloy and only two large grains were obtained in the 15Al alloy,



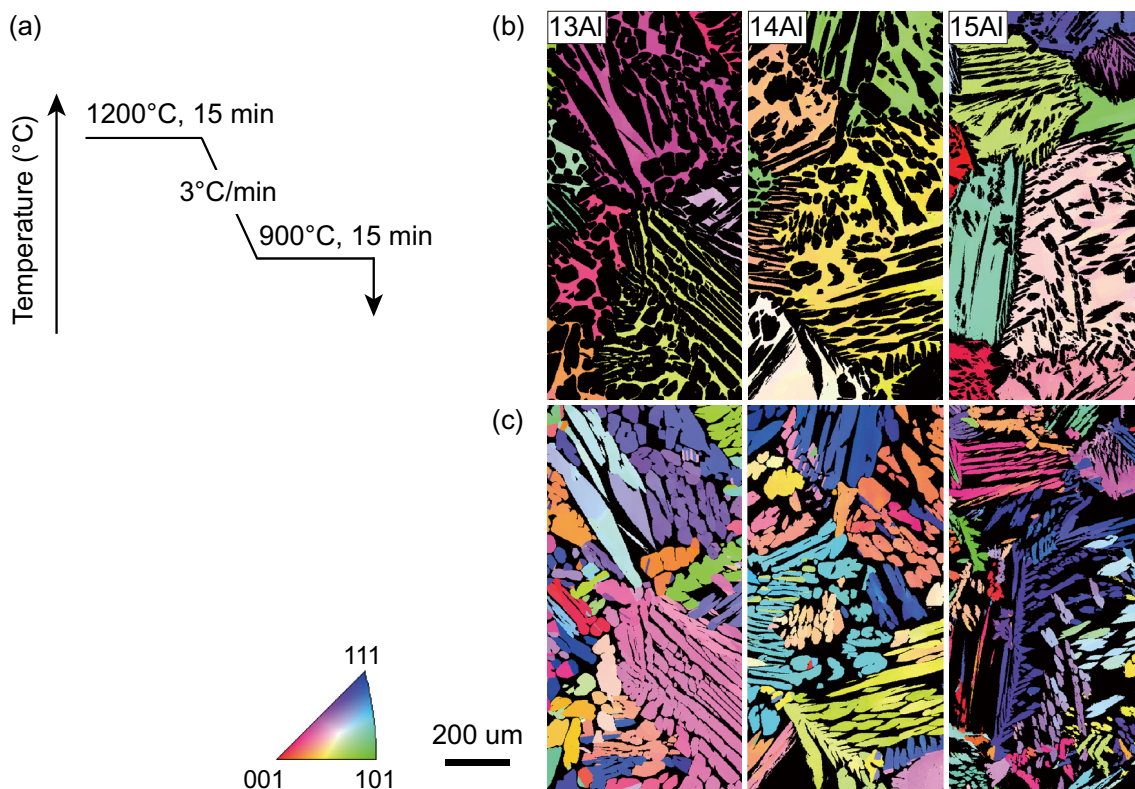


**Fig. 3** **a** Heat treatment history diagram. Inverse pole figure (IPF) maps in the normal direction for **b** BCC and **c** FCC phases quenched from 900 °C for alloys studied in this work

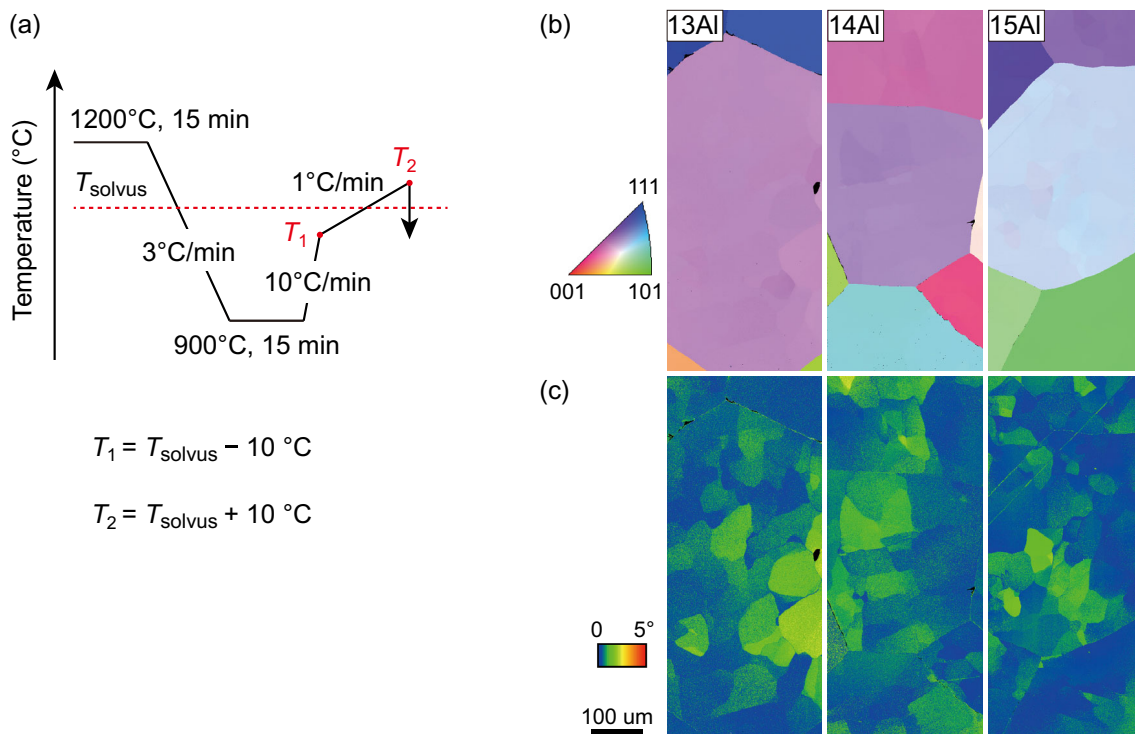


**Fig. 4** **a** Heat treatment history diagram. **b** Inverse pole figure (IPF) maps in the normal direction and **c** grain reference orientation deviation (GROD) maps of BCC phase taken from the alloys

quenched from  $T_2$ , which is a temperature 10 °C higher than  $T_{\text{solvus}}$ , during the final heating process

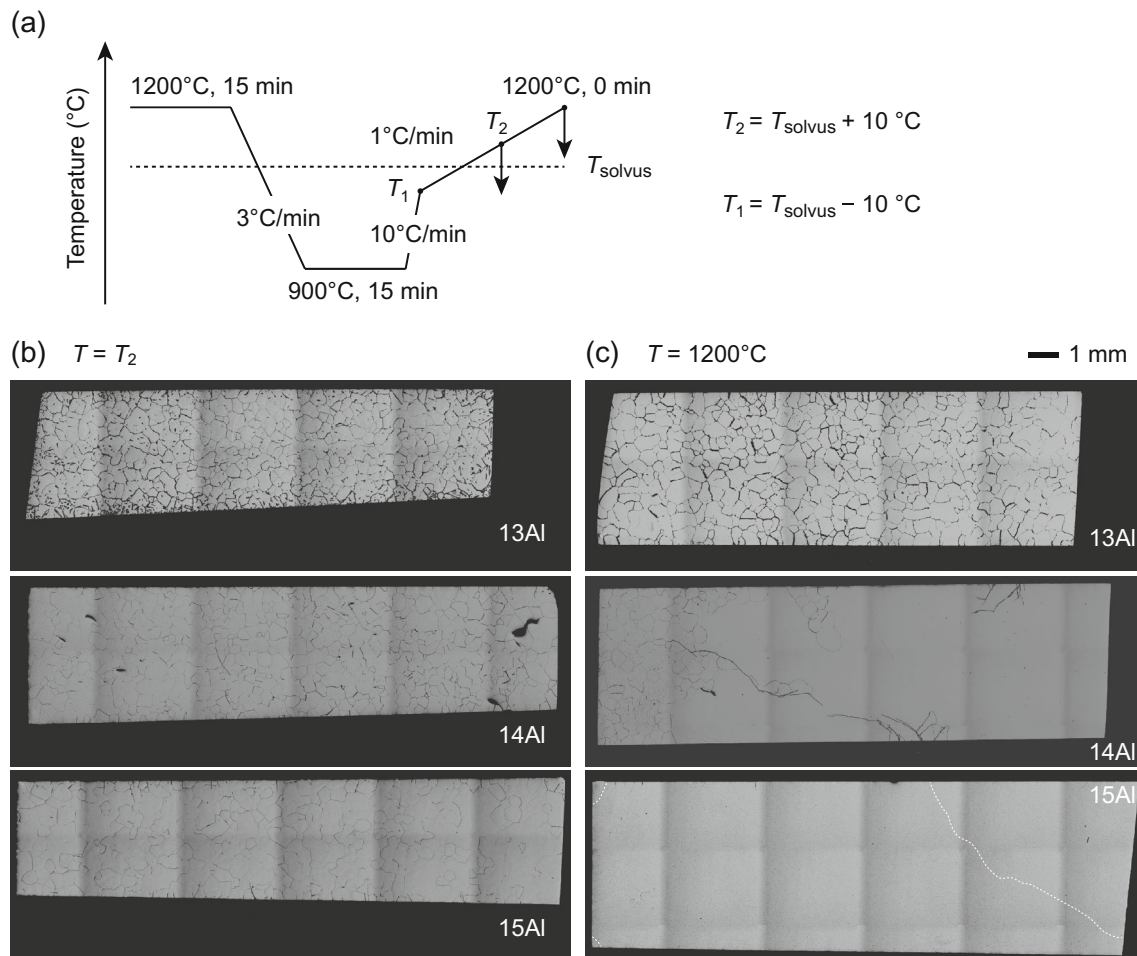


**Fig. 5** Optical microstructure of samples during AGG. **a** Heat treatment history diagram. Optical microstructures taken from samples quenched from **b**  $T_2$  and **c** 1200 °C during the final heating process

whereas no abnormal grains were observed in the 13Al alloy (Fig. 5c). These results show that AGG occurs more readily for alloys with a lower solvus temperature, which is consistent with the trend observed in the quaternary alloy [38]. Single crystals of 60 mm in length were easily fabricated by cyclic heat treatment for the 14Al alloy. Here, we want to emphasize that the efficiencies for single-crystal manufacturing in the 14Al and 15Al alloys are higher than that in the conventional Fe–34Mn–13.5Al–3Cr–7.5Ni alloy, which has about 40 °C higher solvus temperature than that of 14Al alloy [47].

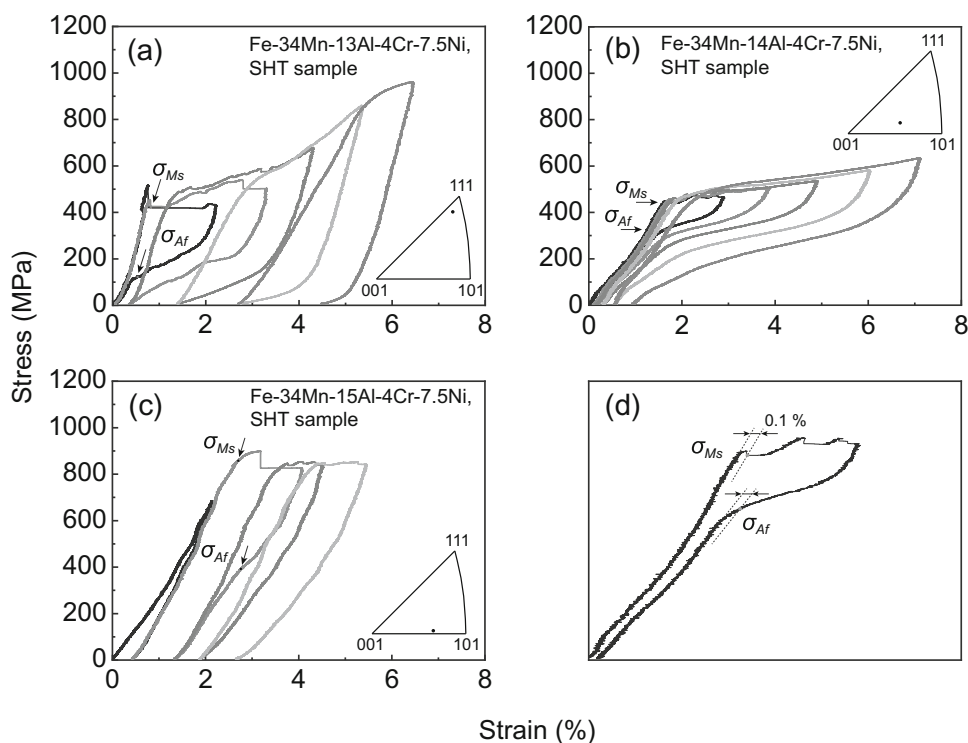
To obtain a larger single crystal through AGG, the driving force for AGG needs to be increased and the generation frequency of abnormal grains needs to be reduced [33, 38]. It can be easily understood that the finer FCC precipitates in a lower solvus temperature alloy (for example, 15Al alloys in the present work and Fe–34Mn–17Al–7.5Ni in Ref. 38) result in finer subgrain structures in the BCC phase, leading to a larger driving force. On the other hand, a large single crystal could not be obtained

easily for the 13Al alloy with the highest solvus temperature, despite the moderately fine subgrain structure (Fig. 4). This result may be related to the generation frequency of abnormal grains [33, 38]. Further systematic investigation of AGG in this alloy system is necessary. It is concluded that by a proper adjustment of the solvus temperature, single crystals can be easily obtained in a quinary alloy system.

### Superelasticity

To evaluate the superelastic performance of these 4Cr alloys, single-crystal samples obtained by AGG were prepared and incremental compression tests were carried out at room temperature. Figure 6 shows the stress-strain curves of the single-crystal samples with different compositions. All the samples tested were SHT samples, which means that no further aging treatment was conducted after the cyclic heat treatment. Note that the crystal orientations in the compression direction are different among the

**Fig. 6 a–c** Compressive stress-strain curves acquired at room temperature. The compression orientation of each single-crystal is indicated in the inset figure. The critical stress for forward martensitic transformation starting stress  $\sigma_{Ms}$  and reverse martensitic transformation finishing stress  $\sigma_{Af}$  are indicated by arrows; values were determined by 0.1% strain offset method. **d** An example demonstrating the determination of the critical stress through 0.1% strain offset method



samples. As shown in Fig. 6, 13Al showed perfect shape recovery up to a strain of 2%, but a remarkable residual strain was observed upon increasing the applied strain. The 14Al alloy, however, exhibited a higher critical stress than 13Al, and its recovery strain was approximately 5%. One possible reason causing this change in superelastic strain is the difference in the compression direction, that is, the transformation strain of the 13Al sample in the  $\langle 111 \rangle$  direction is smaller [45]. On the other hand, 15Al only showed a small recovery strain in the second cycle, as indicated by the arrow in Fig. 6c. This means that the critical stress of slip deformation in the parent phase is approximately 800 MPa, which is lower than the forward martensitic transformation starting stress,  $\sigma_{Ms}$ . As shown in Fig. 6, for the 13Al and 14Al alloys, both the  $\sigma_{Ms}$  and the reverse martensitic transformation finishing stress,  $\sigma_{Af}$ , which are defined as shown in Fig. 6d, increased with increasing Al composition. Moreover, the  $\sigma_{Ms}$  of 15Al was above 800 MPa, which is much higher than that of 14Al.

The increase in the critical stress from 13Al to 14Al is smaller than that from 14Al to 15Al, but direct comparison of the superelastic properties of single-crystal samples with different compositions is generally difficult because the transformation critical stress,  $\sigma_c$ , depends not only on the transformation temperature, but also on the crystal orientation. This relationship is defined by the Clausius-Clapeyron equation:

$$\frac{d\sigma_c}{dT} = -\frac{\Delta S}{\varepsilon V_m}, \quad (1)$$

where  $d\sigma_c/dT$  is the temperature-dependence of the critical stress,  $\Delta S$  is the entropy change during the martensitic transformation,  $V_m$  is the molar volume, and  $\varepsilon$  is the transformation strain. In the Fe–Mn–Al–Ni-based alloys, the compression along the  $\langle 111 \rangle$  direction tends to have lower transformation strain and thus higher critical stress ( $\sigma_{Ms}$ ) [29, 45]. As shown in Fig. 6, the compression orientation of 13Al is close to the  $\langle 111 \rangle$  direction with small transformation strain,  $\varepsilon$ , while those of 14Al and 15Al are close to each other and between the  $\langle 100 \rangle$  and  $\langle 110 \rangle$  directions with larger  $\varepsilon$ . From Eq. (1), the  $\sigma_c$  in 13Al should be lower for a similar orientation to 14Al and 15Al samples. Therefore, when the effect of orientation is excluded, there is a clear tendency for both  $\sigma_{Ms}$  and  $\sigma_{Af}$  to increase with increasing Al content. This means that  $\sigma_c$  at a certain orientation and the thermodynamic stability of the parent phase increase with Al addition. Note that the recovery strain of superelasticity may become small for a large  $\varepsilon$  orientation in 13Al because of low  $\sigma_{Af}$ . In this sense, 14Al seems to be better to obtain a large recovery strain.

Figure 7 shows the phase diagram of the Fe–34Mn– $x$ Al–4Cr–7.5Ni alloy, calculated using the CALPHAD method. The temperature at which the Gibbs energies of the BCC and FCC phases are equal ( $T_0^{\text{BCC/FCC}}$ ) decreased with increasing Al content, indicating that the BCC phase



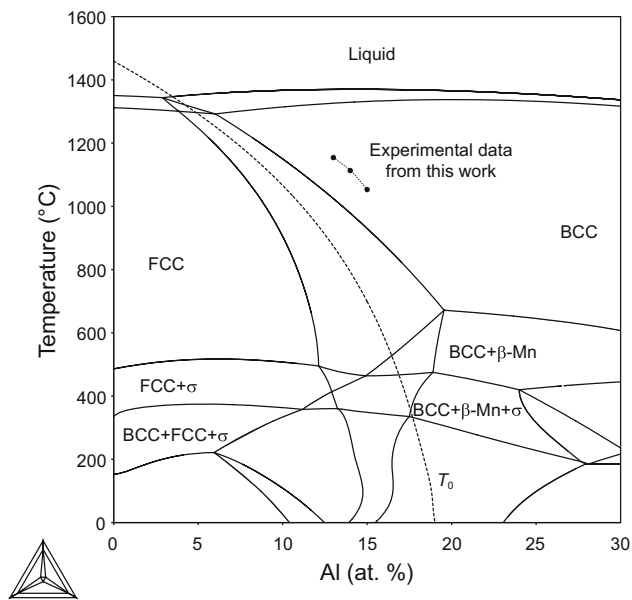


**Fig. 7** Vertical section of Fe–34Mn–*x*Al–4Cr–7.5Ni phase diagram calculated through CALPHAD method using TCFE9 database (Thermo-Calc Software AB). The dashed line indicates the calculated  $T_0^{\text{BCC/FCC}}$  values of this alloy system. The experimentally determined solvus temperatures (BCC + FCC → BCC) are indicated by solid circles

is more stable in the higher Al region. This calculated result is qualitatively in accordance with the results of the compression tests, in which the critical stress increases with increasing Al content, which is consistent with the fact that Al stabilizes the BCC phase to a greater extent than the FCC phase. The calculated  $T_0^{\text{BCC/FCC}}$  temperatures, however, are very high in 13Al to 15Al, suggesting thermal martensitic transformation at high temperatures, although these alloys do not show thermal martensitic transformation in experiments. This may result from the following effects: (1) the accuracy of the calculation, (2) the compositional change of the matrix BCC phase by the precipitation of B2 phase, and (3) the additional energy for the distortion of the B2 precipitates on martensitic transformation [40]. Because the FCC solvus temperatures determined in this study (Fig. 2) are not far from the calculated solvus line plotted in Fig. 7, the latter two effects seem to be the main reasons for the discrepancy. Recently, Walnsch et al. [40] quantitatively discussed the (3) additional energy and pointed out that this energy increases with increasing Al content in the B2-NiAl precipitate. Therefore, it is considered that the increase of Al in this work suppresses the martensitic transformation due to the stabilization of both the BCC matrix and the B2 precipitates. Note that the  $T_0^{\text{BCC/FCC}}$  line gradually becomes vertical in the low-temperature region, which means that the  $\Delta S$  approaches zero [12].

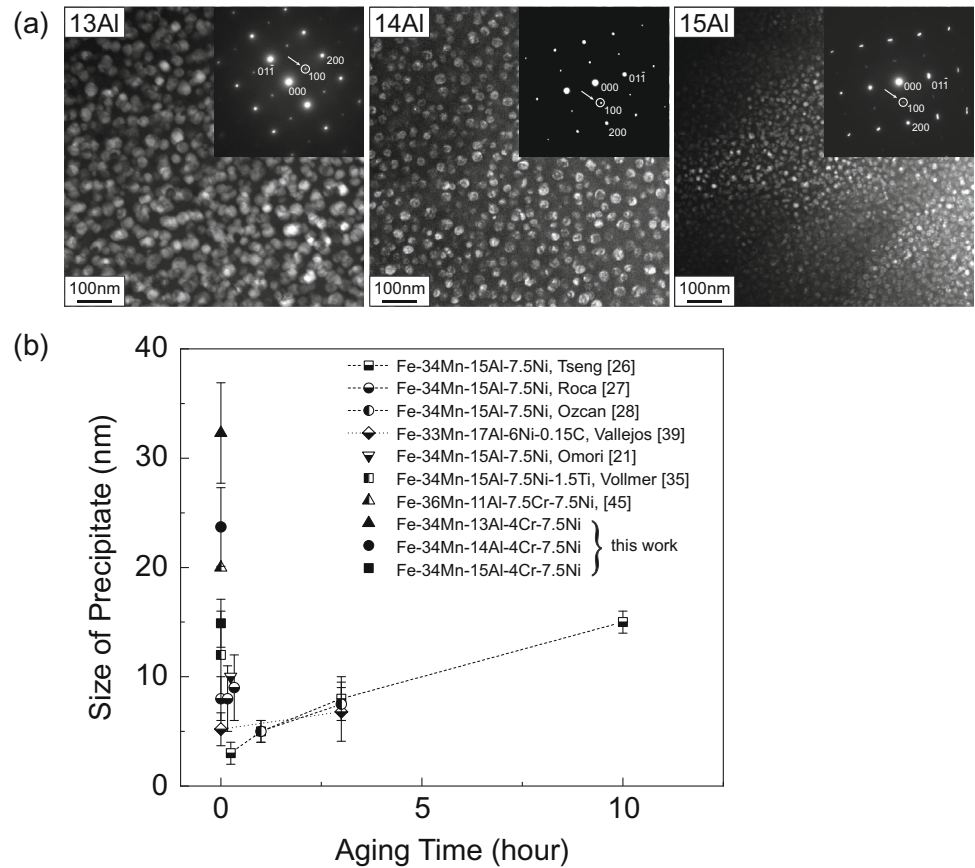
## B2 Precipitates

Since the superelastic behavior in this alloy system is closely related to the B2 coherent precipitates, TEM was used to observe this precipitation in these alloys. Figure 8a shows the TEM dark-field images of 13Al, 14Al, and 15Al, obtained from the selected area diffraction patterns, where the incident beam direction was along  $[011]_{\text{BCC}}$ . The B2 particles precipitated in the disordered BCC (A2) matrix during water quenching from a single phase, as well as in the Fe–Mn–Al–Ni quaternary alloys [27, 39], where the average particle diameters are approximately  $32.3 \pm 4.6$  nm,  $23.7 \pm 3.6$  nm, and  $14.9 \pm 2.2$  nm for 13Al, 14Al, and 15Al, respectively. Previous reports showed that the optimal precipitate size for Fe–Mn–Al–Ni alloy is about 6–10 nm and that larger precipitate size will result in the increase of stress hysteresis and deterioration of superelastic performance due to the coherency loss [22]. Therefore, the increase in Al content in this study should be beneficial to the superelasticity, but the  $\sigma_{Ms}$  of 15Al is too high to achieve superelasticity.

For 14Al alloy, under the same water quenching conditions, its value of precipitate size is comparable to that of the Fe–36Mn–11Al–7.5Cr–7.5Ni alloy [45] and larger than that of Fe–Mn–Al–Ni–Ti [35] and Fe–Mn–Al–Ni [26–28, 39] alloys, as shown in Fig. 8b. The precipitation is attributed to phase separation due to ordering in the BCC phase reported in the Fe–Ni–Al system, where the high-temperature BCC phase decomposes into Fe-rich disordered  $\alpha_1$  (A2) and Ni–Al-rich ordered  $\alpha_2$  (B2) phases during cooling [48]. Hao et al. [49] studied the partition of alloying elements between the  $\alpha_1$  and  $\alpha_2$  phases in Fe–Ni–Al-based alloys and found that Cr mostly distributes to the  $\alpha_1$  phase. A similar result was confirmed by STEM-EDS analysis of the Fe–36Mn–11Al–7.5Cr–7.5Ni alloy [45]. Furthermore, the summit temperature of the  $\alpha_1$  (A2) +  $\alpha_2$  (B2) two-phase region in the Cr–NiAl pseudo-binary system was higher than that in the Fe–NiAl system [50]. Consequently, owing to the widening of the miscibility gap to a higher temperature, the addition of Cr to the Fe–Mn–Al–Ni alloy causes precipitation of the B2 phase to begin at higher temperatures, and thus the particle size may become larger. The large precipitate size, however, obviously has a negative impact on the superelasticity because of the introduction of dislocations owing to the coherence loss between the matrix and precipitate during martensitic transformation. To improve the superelasticity, a further tailoring of the composition aiming to refine the size of the precipitate is necessary, for instance, by reducing the Ni content [39].



**Fig. 8 a** Dark-field images taken from 100 reflection in SHT 13Al, 14Al, and 15Al alloys. The insets of (a) are the selected area diffraction patterns. **b** A Summary of the size of B2 precipitate in diameter for the Fe–Mn–Al–Ni-based alloys [21, 26–28, 35, 39, 45]



### Temperature-Dependence of SE

To confirm the temperature-dependence of the critical stress, compression tests were conducted at an applied strain of 1.6% at various temperatures (10 – 300 K) for the 14Al alloy, which shows the best superelastic property and a higher AGG efficiency. As shown in the stress–strain curves in Fig. 9a, at all temperatures evaluated, almost complete superelasticity was obtained. For all the samples,

fine serrations were detected (except at 10 K), mainly in the loading process. Similar behavior has been reported for Ni–Co–Mn–In [51] and Fe–Mn–Al–Ni [23, 52] alloys, which may be caused by the nucleation or intermittent growth of stress-induced martensite plates [53]. The complicated and large serration at 10 K may also have the same origin, but the amplitude may be enhanced by the low specific heat at low temperatures [45]. The transformation stresses,  $\sigma_{Ms}$  and  $\sigma_{Af}$ , are shown in Fig. 9b. The equilibrium

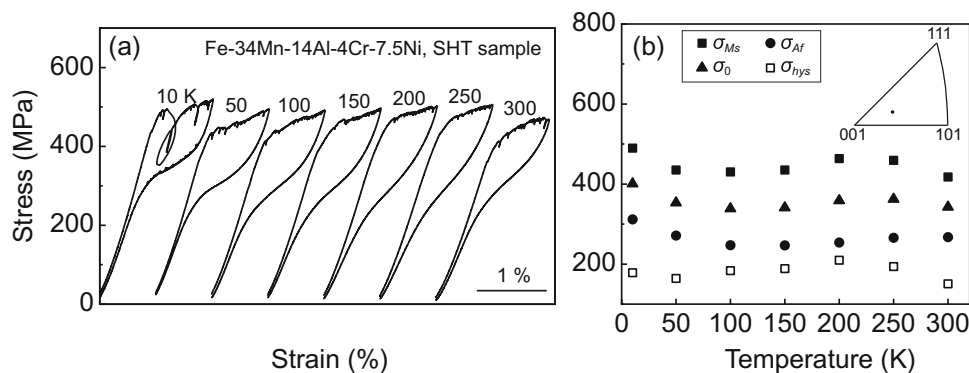


**Fig. 9 a** Stress–strain curves obtained from compression tests at various temperatures for single-crystal Fe–34Mn–14Al4Cr–7.5Ni (14Al) alloy. **b** Temperature-dependence of the critical stress for forward martensitic transformation starting stress  $\sigma_{Ms}$  (square),

reverse martensitic transformation finishing stress  $\sigma_{Af}$  (dot), equilibrium stress  $\sigma_0$  ( $= (\sigma_{Ms} + \sigma_{Af})/2$ , triangle), and transformation hysteresis  $\sigma_{hys}$  ( $= \sigma_{Ms} - \sigma_{Af}$ , open square). Compression orientation is indicated in the inset figure

stress ( $\sigma_0$ ) and the stress hysteresis ( $\sigma_{hys}$ ) do not change significantly with the variation in temperature, which is similar to the previous results for the conventional Fe<sub>34</sub>Mn–3.5Al–3Cr–7.5Ni [45]. The temperature-dependence of the critical stress was estimated to be  $-0.095$  MPa/K by linear fitting of  $\sigma_0$  from  $-263$  °C (10 K) to  $27$  °C (300 K), where this value is close to that of conventional Fe–34Mn–13.5Al–3Cr–7.5Ni (10–300 K,  $0.085$  MPa/K) [45].

The results of this study demonstrate that this new 14Al alloy has a higher critical stress, a near-zero temperature-dependent superelasticity, and a high efficiency for single-crystal manufacturing, compared with the conventional Fe–34Mn–13.5Al–3Cr–7.5Ni [45]. In addition, the Fe–Mn–Al–Cr–Ni alloys are expected to exhibit better corrosion resistance than the Fe–Mn–Al–Ni alloys. Recently, the corrosion behavior of quaternary Fe–Mn–Al–Ni in NaCl [54] and NaCl-contaminated Ca(OH)<sub>2,sat</sub> solutions [55] was investigated. It has also been reported that the addition of Cr improves the anti-corrosion behavior of high-Mn TWIP steels [56]. In this study, etching was more difficult in the Cr-added Fe–Mn–Al–Ni alloys compared with the quaternary Fe–Mn–Al–Ni alloys. It is expected that the addition of Cr can also improve the corrosion resistance.

## Conclusions

In this study, the microstructure and superelastic performance of Fe–34Mn–*x*Al–4Cr–7.5Ni shape memory alloys with different Al contents were investigated. Based on the experimental results, the following conclusions are drawn:

1. The addition of Al decreases the FCC solvus temperature and results in finer FCC precipitates at  $900$  °C. It is easier to obtain large grains in alloys with a higher Al content through AGG induced by cyclic heat treatment. The efficiencies for single-crystal manufacturing in the 14Al (Fe–34Mn–14Al–4Cr–7.5Ni) and 15Al (Fe–34Mn–15Al–4Cr–7.5Ni) alloys seem to be higher than that in the conventional Fe–34Mn–13.5Al–3Cr–7.5Ni alloy with near-zero temperature-dependence on critical stress.

2. The alloys with higher Al content exhibit a higher critical stress for martensitic transformation. The 13Al (Fe–34Mn–13Al–4Cr–7.5Ni) and 14Al alloys exhibit superelasticity, but plastic deformation occurs instead of superelasticity in 15Al because of its high critical stress.

3. The average diameters of the precipitates decrease with increasing Al content and are approximately  $32.3$  nm,  $23.7$  nm, and  $14.9$  nm in the SHT 13Al, 14Al, and 15Al samples, respectively. The relatively small precipitate size may positively influence the superelastic performance of 14Al.

4. The 14Al alloy shows superelasticity from cryogenic temperature to room temperature. The temperature-dependence of the critical stress for superelasticity was very low ( $-0.095$  MPa/K).

5. The stability of the BCC phase and the FCC solvus temperature are important factors in the design of Fe–Mn–Al–Ni-based shape memory alloys with regard to single crystallization by AGG and the superelastic performance. Considering these factors, the 14Al is the optimal composition among the Fe–Mn–Al–Cr–Ni alloys in this study. A single crystal is easier to be obtained in this alloy than for conventional Fe–34Mn–13.5Al–3Cr–7.5Ni alloys. The critical stress is higher, but the temperature-dependence is nearly zero.

6. The average diameter of the precipitates in the SHT 14Al sample is close to that of a previously reported Fe–36Mn–11Al–7.5Cr–7.5Ni alloy and larger than that for the Fe–34Mn–15Al–7.5Ni quaternary alloy under the same heat treatment conditions. In order to obtain better superelasticity, further composition tailoring aiming to suppress the size of the precipitate is necessary.

**Acknowledgements** This study was supported by JSPS KAKENHI grant 15H05766. JX appreciates the experimental support provided by Dr. K. Kobayashi.

## References

1. Dunne DP, Wayman CM (1973) The effect of austenite ordering on the martensite transformation in Fe–Pt alloys near the composition Fe<sub>3</sub>Pt: I. Morphology and transformation characteristics Metall Trans 4:137–145
2. Sohmura T, Oshima R, Fujita FE (1980) Thermoelastic FCC–FCT martensitic transformation in Fe–Pd alloy. Scr Metall 14:855–856
3. Maki T, Kobayashi K, Minato M, Tamura I (1984) Thermoelastic martensite in an ausaged Fe–Ni–Ti–Co alloy. Scr Metall 18:1105–1109
4. Tanaka Y, Himuro Y, Kainuma R et al (2010) Ferrous polycrystalline shape-memory alloys showing huge superelasticity. Science 327:1488–1490
5. Omori T, Abe S, Tanaka Y et al (2013) Thermoelastic martensitic transformation and superelasticity in Fe–Ni–Co–Al–Nb–B polycrystalline alloy. Scr Mater 69:812–815
6. Lee D, Omori T, Kainuma R (2014) Ductility enhancement and superelasticity in Fe–Ni–Co–Al–Ti–B polycrystalline alloy. J Alloys Compd 617:120–123
7. Sato A, Chishima E, Soma K, Mori T (1982) Shape memory effect in  $\gamma\rightleftharpoons\epsilon$  transformation in Fe–30Mn–1Si alloy single crystals. Acta Metall 30:1177–1183
8. Sawaguchi T, Maruyama T, Otsuka H et al (2016) Design concept and applications of Fe–Mn–Si-based alloys—from shape-memory to seismic response control. Mater Trans 57:283–293
9. La Roca P, Baruj A, Sade M (2017) Shape-memory effect and pseudoelasticity in Fe–Mn-based alloys. Shape Mem Superelasticity 3:37–48
10. Omori T, Watanabe K, Umetsu RY et al (2009) Martensitic transformation and magnetic field-induced strain in Fe–Mn–Ga shape memory alloy. Appl Phys Lett 95:27–30

11. Zhu W, Liu EK, Feng L et al (2009) Magnetic-field-induced transformation in FeMnGa alloys. *Appl Phys Lett* 95:e222512
12. Omori T, Ando K, Okano M et al (2011) Superelastic effect in polycrystalline ferrous alloys. *Science* 333:68–71
13. Lee D, Omori T, Han K et al (2018) Effect of thermomechanical processing on texture and superelasticity in Fe–Ni–Co–Al–Ti–B alloy. *Shape Mem Superelasticity* 4:102–111
14. Zhang C, Zhu C, Shin S, Vecchio K (2018) Enhancement of <001> recrystallization texture in non-equiatomic Fe–Ni–Co–Al–based high entropy alloys by combination of annealing and Cr addition. *J Alloys Compd* 768:277–286
15. Lee D, Omori T, Han K et al (2020) Texture formation in a polycrystalline Fe–Ni–Co–Al–Ti–B shape memory alloy. *ISIJ Int* 60:2973–2982
16. Sobrero CE, Lauhoff C, Wegener T et al (2020) On the impact of texture and grain size on the pseudoelastic properties of polycrystalline Fe–Ni–Co–Al–Ti alloy. *Shape Mem Superelasticity* 6:191–201
17. Ma J, Hornbuckle BC, Karaman I et al (2013) The effect of nanoprecipitates on the superelastic properties of FeNiCoAlTa shape memory alloy single crystals. *Acta Mater* 61:3445–3455
18. Tseng LW, Ma J, Karaman I et al (2015) Superelastic response of the FeNiCoAlTi single crystals under tension and compression. *Scr Mater* 101:1–4
19. Chumlyakov YI, Kireeva IV, Kuts OA et al (2015) Shape memory effect and superelasticity in [001] single crystals of Fe–Ni–Co–Al–Nb(B) ferromagnetic alloy. *Russ Phys J* 58:889–897
20. Ando K, Omori T, Ohnuma I et al (2009) Ferromagnetic to weak-magnetic transition accompanied by bcc to fcc transformation in Fe–Mn–Al alloy. *Appl Phys Lett* 95:e212504
21. Omori T, Nagasako M, Okano M et al (2012) Microstructure and martensitic transformation in the Fe–Mn–Al–Ni shape memory alloy with B2-type coherent fine particles. *Appl Phys Lett* 101:e231907
22. Tseng LW, Ma J, Wang SJ et al (2015) Superelastic response of a single crystalline FeMnAlNi shape memory alloy under tension and compression. *Acta Mater* 89:374–383
23. Xia J, Xu X, Miyake A et al (2017) Stress- and magnetic field-induced martensitic transformation at cryogenic temperatures in Fe–Mn–Al–Ni shape memory alloys. *Shape Mem Superelasticity* 3:467–475
24. Omori T, Okano M, Kainuma R (2013) Effect of grain size on superelasticity in Fe–Mn–Al–Ni shape memory alloy wire. *APL Mater* 1:e032103
25. Tseng LW, Ma J, Vollmer M et al (2016) Effect of grain size on the superelastic response of a FeMnAlNi polycrystalline shape memory alloy. *Scr Mater* 125:68–72
26. Tseng LW, Ma J, Hornbuckle BC et al (2015) The effect of precipitates on the superelastic response of [100] oriented FeMnAlNi single crystals under compression. *Acta Mater* 97:234–244
27. La Roca P, Baruj A, Sobrero CE et al (2017) Nanoprecipitation effects on phase stability of Fe–Mn–Al–Ni alloys. *J Alloys Compd* 708:422–427
28. Ozcan H, Ma J, Wang SJ et al (2017) Effects of cyclic heat treatment and aging on superelasticity in oligocrystalline Fe–Mn–Al–Ni shape memory alloy wires. *Scr Mater* 134:66–70
29. Tseng LW, Ma J, Wang SJ et al (2016) Effects of crystallographic orientation on the superelastic response of FeMnAlNi single crystals. *Scr Mater* 116:147–151
30. Poklonov VV, Chumlyakov YI, Kireeva IV, Kirillov VA (2018) Superelastic response in <1 2 2>-oriented single crystals of FeMnAlNi shape memory alloy in tension and compression. *Mater Lett* 233:195–198
31. Tseng LW, Ma J, Chumlyakov YI, Karaman I (2019) Orientation dependence of superelasticity in FeMnAlNi single crystals under compression. *Scr Mater* 166:48–52
32. Omori T, Kusama T, Kawata S et al (2013) Abnormal grain growth induced by cyclic heat treatment. *Science* 341:1500–1502
33. Kusama T, Omori T, Saito T et al (2017) Ultra-large single crystals by abnormal grain growth. *Nat Commun* 8:354
34. Omori T, Iwaizako H, Kainuma R (2016) Abnormal grain growth induced by cyclic heat treatment in Fe–Mn–Al–Ni superelastic alloy. *Mater Des* 101:263–269
35. Vollmer M, Arold T, Kriegel MJ et al (2019) Promoting abnormal grain growth in Fe-based shape memory alloys through compositional adjustments. *Nat Commun* 10:2337
36. Vollmer M, Bauer A, Frenck J-M et al (2021) Novel prestressing applications in civil engineering structures enabled by Fe–Mn–Al–Ni shape memory alloys. *Eng Struct* 241:e112430
37. Vollmer M, Krooß P, Karaman I, Niendorf T (2017) On the effect of titanium on quenching sensitivity and pseudoelastic response in Fe–Mn–Al–Ni-base shape memory alloy. *Scr Mater* 126:20–23
38. Xia J, Omori T, Kainuma R (2020) Abnormal grain growth in Fe–Mn–Al–Ni shape memory alloy with higher Al content. *Scr Mater* 187:355–359
39. Vallejos JM, Giordana MF, Sobrero CE, Malarria JA (2020) Excellent pseudoelasticity of Al-rich Fe–33Mn–17Al–6Ni–0.15C (at%) shape memory single crystals obtained without an aging conditioning stage. *Scr Mater* 179:25–29
40. Walnsch A, Kriegel MJ, Motylenko M et al (2021) Thermodynamics of martensite formation in Fe–Mn–Al–Ni shape memory alloys. *Scr Mater* 192:26–31
41. Walnsch A, Kriegel MJ, Fischer PDB et al (2021) Nanoscale twinning and superstructures of martensite in the Fe–Mn–Al–Ni system. *Materialia* 16:e101062
42. Umino R, Liu XJ, Sutou Y et al (2006) Experimental determination and thermodynamic calculation of phase equilibria in the Fe–Mn–Al system. *J Phase Equilibria Diffus* 27:54–62
43. Villars, P, Prince, A, Okamoto, H (eds) 1995 Handbook of ternary alloy phase diagrams, Materials Park (Ohio), American Society for Metals, 7:8777
44. Noguchi Y, Omori T, Kainuma R (2017) Effects of Cr on martensitic transformation and oxidation resistance in Fe–Mn–Al–Ni alloys. In: International conference on martensitic transformations (ICOMAT-2017)
45. Xia J, Noguchi Y, Xu X et al (2020) Iron-based superelastic alloys with near-constant critical stress temperature dependence. *Science* 369:855–858
46. Ozcan H (2018) Private Communication
47. Xia J (2021) Development of novel Fe–Mn–Al–Ni based superelastic alloy system with tunable temperature-dependence on transformation stress. Doctor Thesis, Tohoku University.
48. Hao SM, Takayama T, Ishida K, Nishizawa T (1984) Miscibility gap in Fe–Ni–Al and Fe–Ni–Al–Co systems. *Metall Trans A* 15:1819–1828
49. Hao SM, Ishida K, Nishizawa T (1985) Role of alloying elements in phase decomposition in alnico magnet alloys. *Metall Trans A* 16:179–185
50. Kainuma R, Ise M, Ishikawa K et al (1998) Phase equilibria and stability of the B2 phase in the Ni–Mn–Al and Co–Mn–Al systems. *J Alloys Compd* 269:173–180
51. Niitsu K, Xu X, Umetsu RY, Kainuma R (2013) Stress-induced transformations at low temperatures in a Ni<sub>45</sub>Co<sub>5</sub>Mn<sub>36</sub>In<sub>14</sub> metamagnetic shape memory alloy. *Appl Phys Lett* 103:e242406
52. Ozcan H, Ma J, Karaman I et al (2018) Microstructural design considerations in Fe–Mn–Al–Ni shape memory alloy wires: Effects of natural aging. *Scr Mater* 142:153–157
53. Abuzaid W, Wu Y, Sidharth R, Brenne F, Alkan S, Vollmer M, Krooß P, Niendorf T, Sehitoğlu H (2019) Shape Mem Superelasticity 5:263–277
54. Frenck JM, Vollmer M, Mandel M et al (2021) On the Influence of Microstructure on the Corrosion Behavior of Fe–Mn–Al–Ni

- Shape Memory Alloy in 5.0 wt% NaCl Solution. *Adv Eng Mater* 23:1–9
55. Mandel M, Kietov V, Hornig R et al (2021) On the polarisation and Mott-Schottky characteristics of an Fe-Mn-Al-Ni shape-memory alloy and pure Fe in NaCl-free and NaCl-contaminated Ca(OH)<sub>2</sub> sat solution—A comparative study. *Corros Sci* 179:e109172
56. Yuan X, Zhao Y, Li X, Chen L (2017) Effect of Cr on mechanical properties and corrosion behaviors of Fe-Mn-C-Al-Cr-N TWIP steels. *J Mater Sci Technol* 33:1555–1560

**Publisher's Note** Springer Nature remains neutral with regard to jurisdictional claims in published maps and institutional affiliations.